scientific reports

Check for updates

OPEN

3D metamaterial ultra-wideband absorber for curved surface

Mahdi Norouzi[1], Saughar Jarchi[1], Mohsen Ghaffari-Miab[2], Meisam Esfandiari[1], Ali Lalbakhsh[3,4]✉, Slawomir Koziel[5,6], Sam Reisenfeld[3] & Gholamhosein Moloudian[7]

This paper proposes a three-dimensional metamaterial absorber based on a resistive film patch array to develop a low-cost, lightweight absorber for curved surfaces. An excellent absorption over a large frequency band is achieved through two different yet controllable mechanisms; in the first mechanism, a considerable attenuation in the wave power is achieved via graphite resistive films. The absorption is then intensified through magnetic dipoles created by the surface currents, leading to absorption peaks. The simulation results of the absorber show that a broadband absorption greater than 85% is achieved over 35–400 GHz for both TE and TM polarization waves at normal incidence. The structure has more than 167% and 80% absorption bandwidth above 85% and 90%, respectively. It is shown that the proposed metamaterial absorber is independent of incident wave polarization. In addition, the structure is insensitive to incident angles up to 60° for TE mode and full range angle 90° for TM mode. To describe the physical mechanism of the absorber, E-field, power loss density and surface current distributions on the structure are calculated and shown. Moreover, the oblique incidence absorption efficiency is also explained. This absorber paves the way for practical applications, such as sensing, imaging and stealth technology. In addition, the proposed structure can be extended to terahertz, infrared and optical regions.

The advent of materials with a negative refraction index has led to extensive research in the area of metamaterials over the past decade. Metamaterials are attractive not only for their marvelous electromagnetic properties but also for their diverse current and emerging applications[1], such as transmitters[2], sensors[3], spatial modulators[4], IR camouflage[5], thermophotovoltaic[6], phase modulator[7,8], filter[9] and wireless communication[10] and absorbers[11]. The idea of a substance that absorbs all the radiation waves, regardless of the frequency or incident angle, was introduced a century ago by Planck's law[12]. In order to have a practical metamaterial absorber on uneven structures, the absorber should be independent of the incident wave polarization and angle[13]. In general, reduction of sensitivity to electromagnetic wave polarization can be easily achieved by using the symmetric design of metallic arrays on the surface of the absorber[14].

Conventionally, absorbers have a sandwich structure with multiple layers where absorption is a function of the incident angle for both TE and TM modes[15,16]. Some studies have shown that increasing the angle of incidence negatively affects the impedance matching, resulting in higher reflection, leading to a lower absorption rate[17,18]. As a result, designing a low-cost polarization-insensitive absorber capable of efficiently operating under large angles of incidence has been a challenge. Another recent approach for designing absorbers is based on artificial intelligence (AI) algorithms, as described in Ref.[19]. As can be found in the literature, such AI-based approaches can be built and improved using nature-based algorithms such as particle swarm optimization[20,21], different versions of artificial neural networks[22–31], ant colony[32,33], gray golf optimization[34,35], genetic algorithm[36], or other multi-objective optimization algorithms[37–40].

This paper presents a polarization-insensitive absorber composed of resistive films along with a conductive backplate. In this design, resistive metamaterial films are used to create a lossy environment to achieve a broadband response with high absorption up to 60° and 90° for TE and TM mode radiation angles, respectively. Furthermore, the proposed absorber is a suitable candidate for the curvatures thanks to its stable performance for large incident angles.

[1]Faculty of Technical and Engineering, Imam Khomeini International University, Qazvin, Iran. [2]Faculty of Electrical and Computer Engineering, Tarbiat Modares University, Tehran, Iran. [3]School of Engineering, Macquarie University, Sydney, Australia. [4]School of Electrical and Data Engineering, University of Technology Sydney (UTS), Sydney, NSW, Australia. [5]Department of Engineering, Reykjavik University, 102 Reykjavik, Iceland. [6]Faculty of Electronics, Telecommunications and Informatics, Gdansk University of Technology, 80-233 Gdansk, Poland. [7]Tyndall National Institute, University College Cork, Cork T12R5CP, Ireland. ✉email: ali.lalbakhsh@mq.edu.au

Design and simulation

Figure 1a,b show the configuration of the proposed absorber consisting of eight 45-degree hollow sections made of graphite, with a thickness of 0.01 mm, a radius of 1.02 mm and a spacing of 0.17 mm, placed on a copper plate (thickness = 0.1 mm). The electric conductivity of graphite is 1000 [S/m], and the electric conductivity of copper is 5.8e + 007 [S/m]. The pizza shape is chosen for this structure because the horizontal films absorb, and other lossy films absorb waves at different angles. The schematic view of TE and TM mode is shown in Fig. 1c.

The structure has central symmetry and is expected to be non-sensitive to the input wave polarization. Over the past decade, several computational approaches have been successfully applied to optics and electromagnetic problems, such as finite element[41–49], finite difference time domain[50–65], and finite-difference frequency domain[66–72]. In this work, the results are predicted using CST Microwave Studio Transient solver, which is based on the Finite Integration Technique (FIT). In simulations, the unit cell is located in the x–y plane and the wave radiates upon it in the z-direction. In this simulation, we use periodic boundary conditions[73].

Result and discussion

The obtained results for the amplitude of absorption coefficients in the frequency range of 35–400 GHz are shown in Fig. 2a. At the resonance frequencies of 57 GHz and 270 GHz, the absorption rate is 99%; however, it is above 85% for 35–400 GHz bandwidth, following the absorption rate determined in Ref.[74]. An EM wave incident onto the surface is reflected and transmitted. Minimizing the reflection coefficient R(W) and the transmission coefficient T(W) results in high absorptivity. The amount of absorption A(W) is considered as[75]:

$$A(W) = 1 - R(W) - T(W). \tag{1}$$

The amount pf transmission is almost zero because the metal ground and reflection coefficient is calculated by:

$$R(W) = \frac{Z(W) - Z_0(W)}{Z(W) + Z_0(W)},$$

where Z(W) and $Z_0(W)$ are the impedances of the metamaterial unitcell absorber and free space, respectively. Therefore, the zero-reflection condition is satisfied when $Z(W) = Z_0(W)$.

The impedance of the proposed metamaterial unitcell is normalized with the impedance of free space in a normal incident, shown in Fig. 2b. As can be seen, when the real part of the impedance is close to unity and the imaginary parts are zero, the amount of absorption becomes high. This is inevitable that the zero-reflection condition differs under TE and TE modes. For instance, at oblique incidence, the reflection coefficients for the TE and TM polarizations are given by:

$$R_{TE} = \frac{Z(W)COS\theta_i - z_0COS\theta_t}{Z(W)COS\theta_i + z_0COS\theta_t}, \tag{2}$$

and

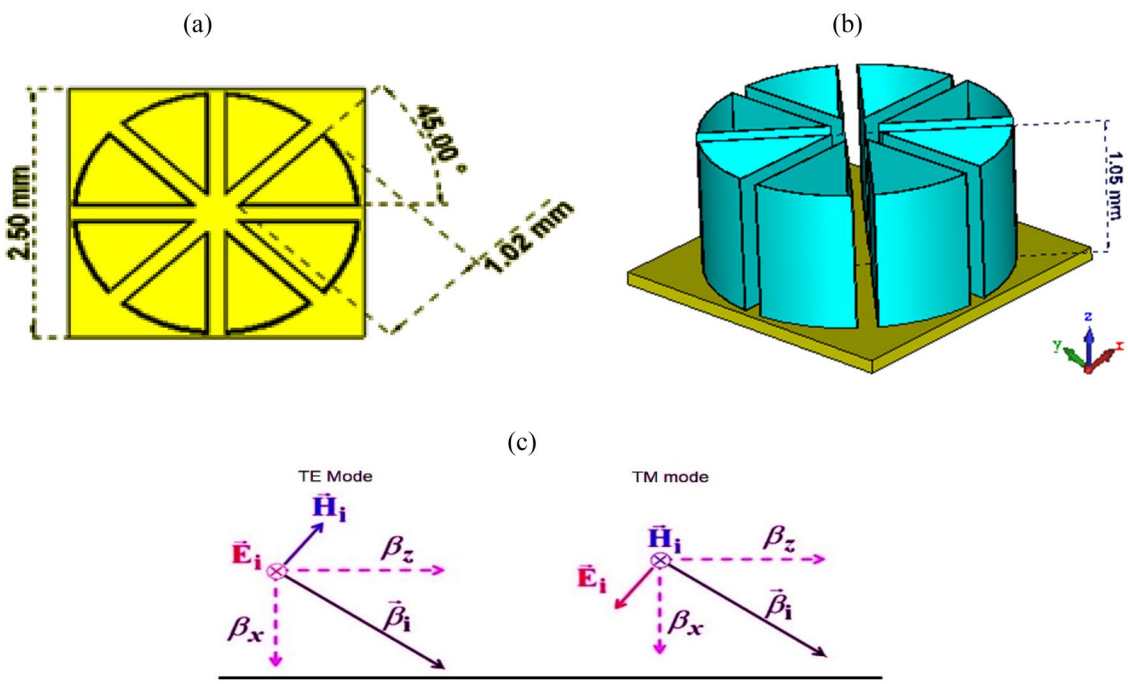

Figure 1. Absorber structure (**a**) top view and (**b**) 3-D view (**c**) schematic view of TE and TM Mode.

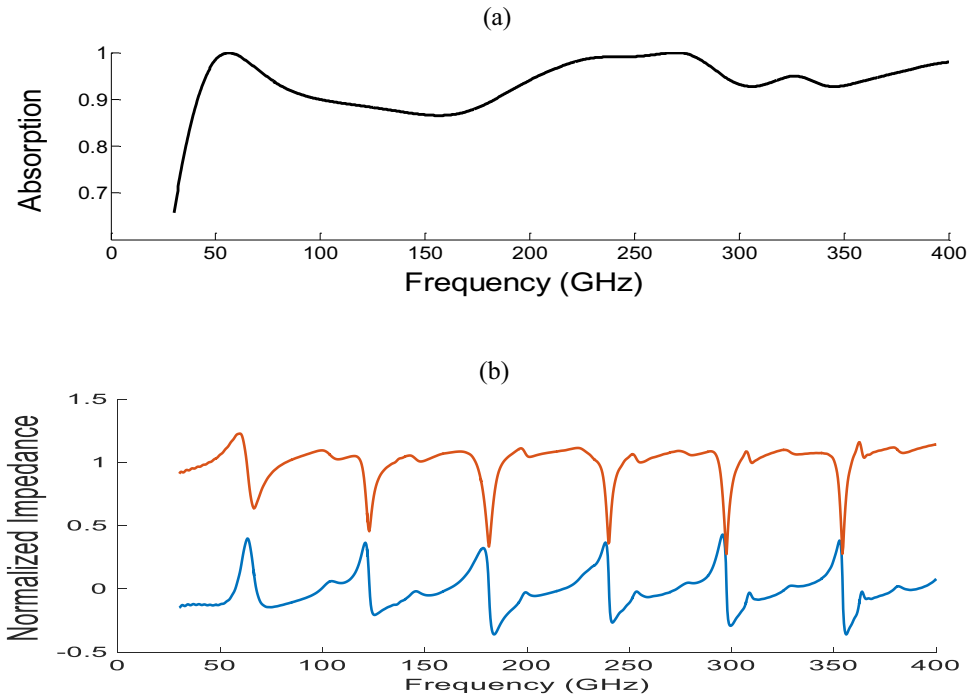

Figure 2. Absorption of the MA with (**a**) the normal incidence and (**b**) normalized impedance of the proposed absorber.

$$R_{TM} = \frac{Z(W)COS\theta_t - Z_0COS\theta_i}{Z(W)COS\theta_t + Z_0COS\theta_i}, \tag{3}$$

where θ_i and θ_t are the incident and transmission angles, respectively. In this situation, the amount of absorption changes when the incident angles are varied.

The reflection curve is investigated for two parameters of width of the unitcell (a) and height of the graphite film (Hg) shown in Fig. 3a,b.

The absorption of the structure for various polarization angles is investigated and demonstrated in Fig. 4. Due to the structure symmetry, the absorber exhibits non-sensitivity to the polarization of the incoming waves. Furthermore, the absorber has nearly zero transmission due to its copper back layer, whose thickness is greater than the skin depth of the incident wave at the entire frequency band.

Absorption mechanism in the normal incident. In order to visualize the absorption mechanism at resonance frequencies, the electrical field distribution for two modes of TE (Ey) and TM (Hy) is shown in Fig. 5. The figure indicates that the electrical field is more concentrated on resistive film edges. This is because both plates form a capacitor and the electric field is higher at the edges of the capacitor.

The power loss density is depicted in Fig. 6. As expected, resistive plates perpendicular to the E direction have a negligible contribution to the power dissipation of the incoming waves. Indeed, the dissipation ratio of the input wave in resistive films depends on their orientation to the direction of the electric field.

Figure 7 provides the absorber surface current distribution at the central frequency of the operating frequency band, giving a better insight into the high absorption of the structure. As shown in this figure, eight parallel current groups are formed along the edges of the film. A magnetic dipole is formed by these eight current loops, creating a magnetic response strongly coupled to E and H input fields, creating high-absorption peaks and ultimately aggravating absorption[76,77]. In conjunction with the primary absorption by the resistive nature of the graphite films, this phenomenon completes the process of absorbing electromagnetic waves in this absorber. To further improve the results, surrogate based optimizations can be as previously used in other electromagnetic devices[78–80].

Absorption in TE and TM modes under oblique incident wave. Figure 8a,b show the absorption diagrams under oblique incidents with different radiation angles (θ). As the incident angle increases, the resonance points are displaced. In detail, the operating frequency band shrinks as the incident angle increases, but absorption remains above 75% for TE mode and is insensitive to incident angle up to 60°. The proposed absorber exhibits more resistance to large incident angles in the case of TM mode, showing a negligible frequency shift.

MOST WIEDZY Downloaded from mostwiedzy.pl

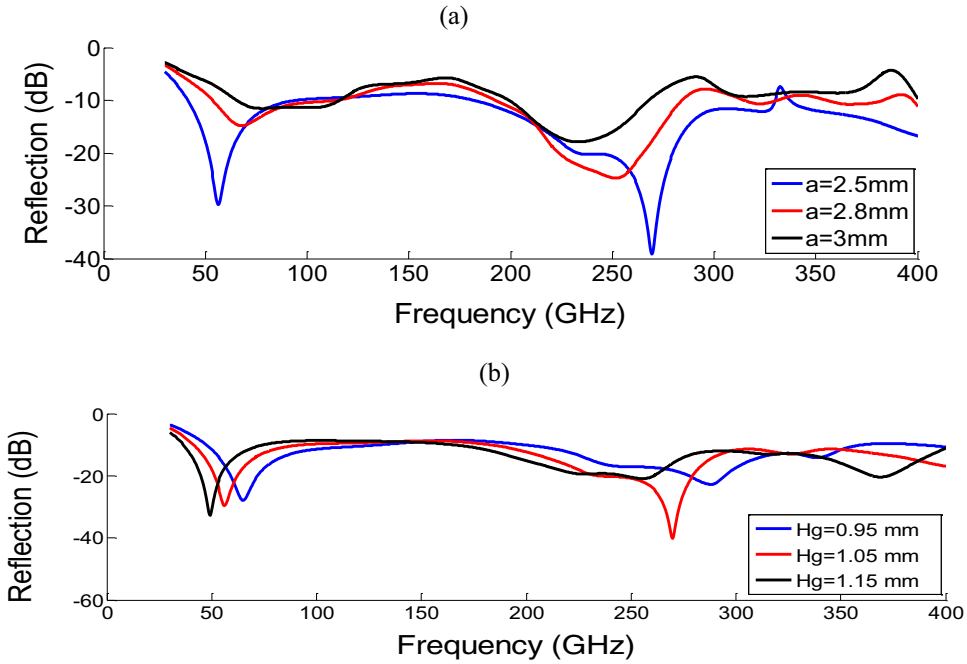

Figure 3. Reflection of the MA with the normal incidence for the physical parameters of (**a**) a (width of the unitcell), Hg = 1.05 and (**b**) Hg (height of the graphite film), a = 2.5.

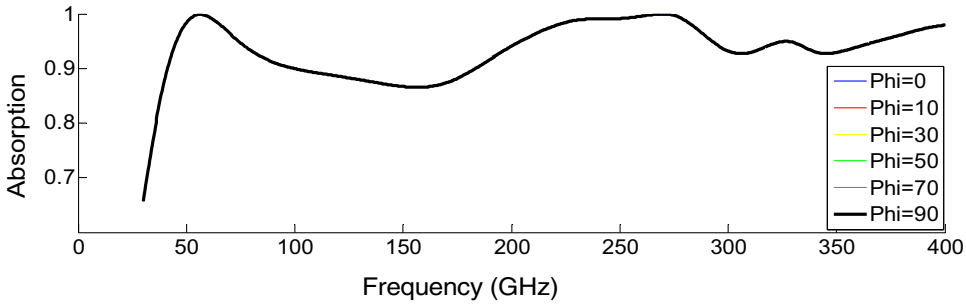

Figure 4. Absorption curves as a function of polarization angle (phi) under the normal incidence with a = 2.5 mm and Hg = 1.05 mm.

Absorption difference mechanism between TE and TM modes. The electric field distribution and power loss density for the incident angles of 10°, 30° and 60° at 220 GHz are shown in Figs. 9 and 10, respectively, highlighting the differences between the input power dissipation in TE and TM modes.

As mentioned, the electric field propagates perpendicular to the resistance films; however, increasing the angle in TM mode makes the electric field component more tangent to the films, leading to more losses. For example, the electric field component at 30° is much more tangent to resistance films than at an angle of 10° (Fig. 9).

In addition, increasing the incident angle for TM mode changes the electric field direction from the single component in the x-direction to two components of x and z. Therefore, unlike the TE mode, the absorption in the TM mode increases as the incident angle increases.

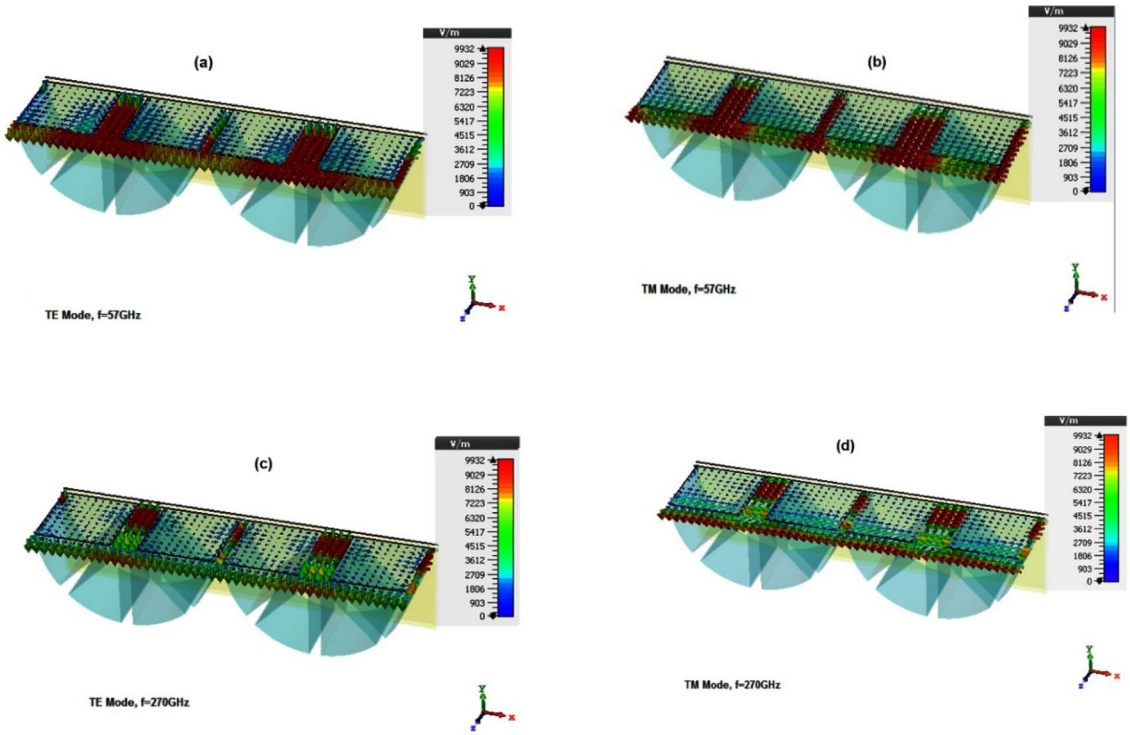

Figure 5. The E-field distributions at (**a**) f = 57 GHz, TE mode (**b**) f = 57 GHz, TM mode (**c**) f = 270 GHz, TE mode and (**d**) f = 270 GHz, TE.

As shown in Fig. 10, for the TE mode (where the electric field remains at all angles in the y-direction), horizontal resistive films (in the x-direction) do not affect the power dissipation because they are aligned perpendicular to the E field.

The effect of absorber on the radar cross section (RCS) of a curved structure. In order to validate the absorber performance in reducing radar cross-section, a curved copper surface is used as shown in Fig. 11a,b. After radiating the electromagnetic wave to the plate, the RCS value is measured. Finally, the absorber coating is fixed on the surface and the RCS measured again and compared with its value in the previous state.

For this purpose, a copper semi-cylinder with a radius of 10 cm, the electrical conductivity of 8.57×10 s/m and a thickness of 0.18 mm was created (Fig. 11a), and a plane wave with the open boundary conditions was radiated to it from the front in the CST software environment. After analyzing the structure, the RCS is obtained at different angles (θ) at the central frequency when the polarization angle is zero. Once again, the surface is covered by the proposed absorber (Fig. 11b), and the RCS results for the two cases are shown in Fig. 12. The comparison between the two graphs shows the RCS is considerably smaller with the absorber, and this RCS reduction is visible at all angles. The RCS comparison diagram shows a difference of as large as 10 dB between the two modes. In fact, when the proposed metamaterial absorber coating covers the curve surface, it is hidden from the radar view and has a 90% reduction in RCS compared to a bare metal plate. Table 1 compares the proposed absorber with some of the recently published works. As can be seen from this table, the proposed absorber is superior to previous structures in terms of bandwidth and sensitivity to the incident wave angle. In addition, it is worth mentioning that the proposed absorber is lightweight, thanks to its graphite-based configuration.

Conclusion

This paper proposes a straightforward yet highly efficient absorber based on graphite resonators that require neither lumped elements nor dielectric substrates, contributing to affordable manufacturing. Furthermore, due to its symmetric geometry, the proposed absorber demonstrates a stable response over a large frequency bandwidth of 167%, regardless of the incoming wave polarization. The absorber is flexible and suitable for curved surfaces, showing acceptable performance under oblique incidents up to 60° and 90° for TE and TM modes, respectively.

MOST WIEDZY Downloaded from mostwiedzy.pl

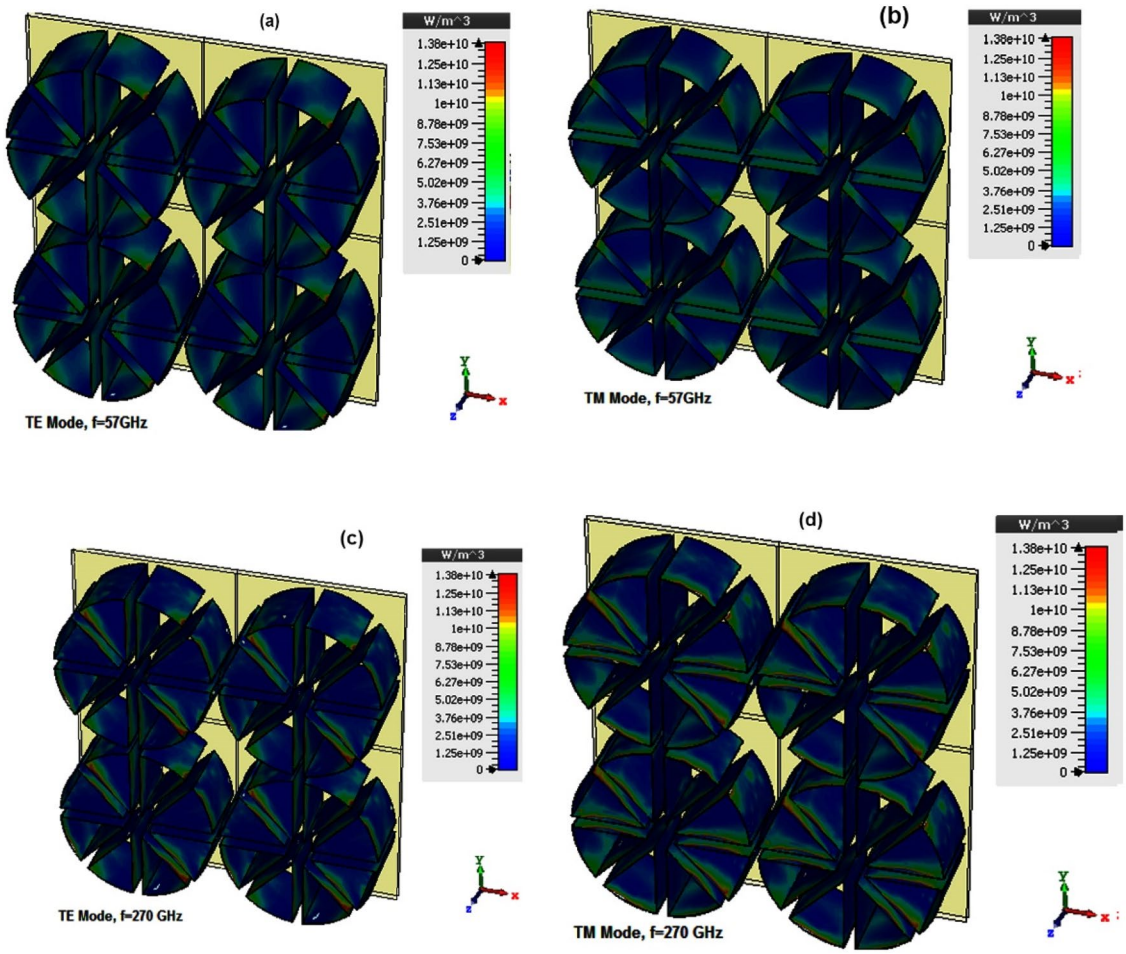

Figure 6. The power loss density at (**a**) f = 57 GHz, TE mode (**b**) f = 57 GHz, TM mode (**c**) f = 270 GHz, TE mode and (**d**) f = 270 GHz, TE mode.

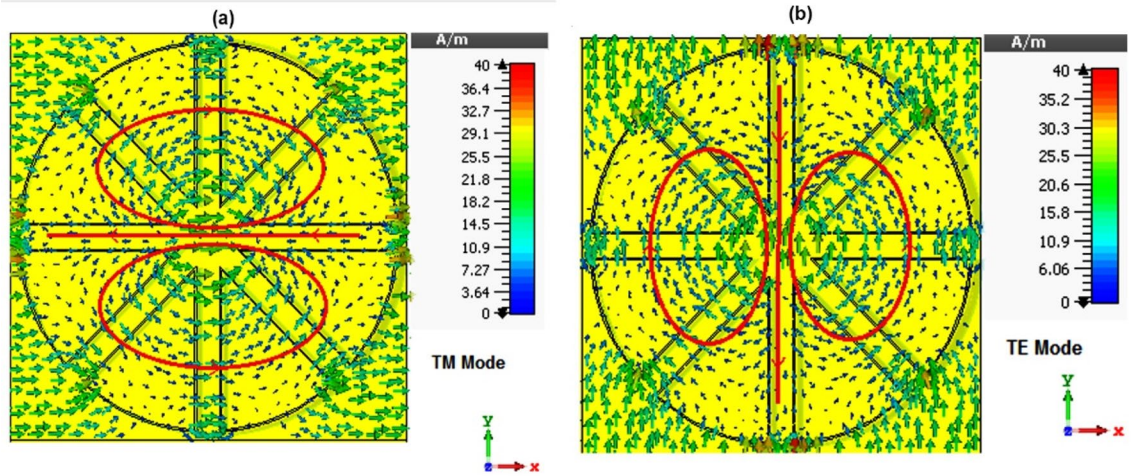

Figure 7. The surface current distribution at the central frequency (220 GHz) for (**a**) TM and (**b**) TE mode.

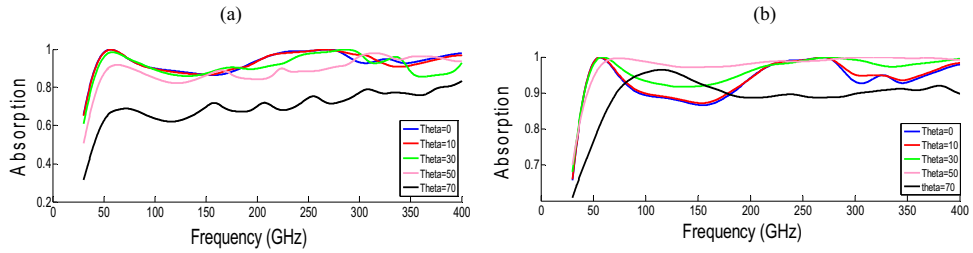

Figure 8. The absorption is based on oblique incidence (theta) (**a**) TE mode (**b**) TM mode.

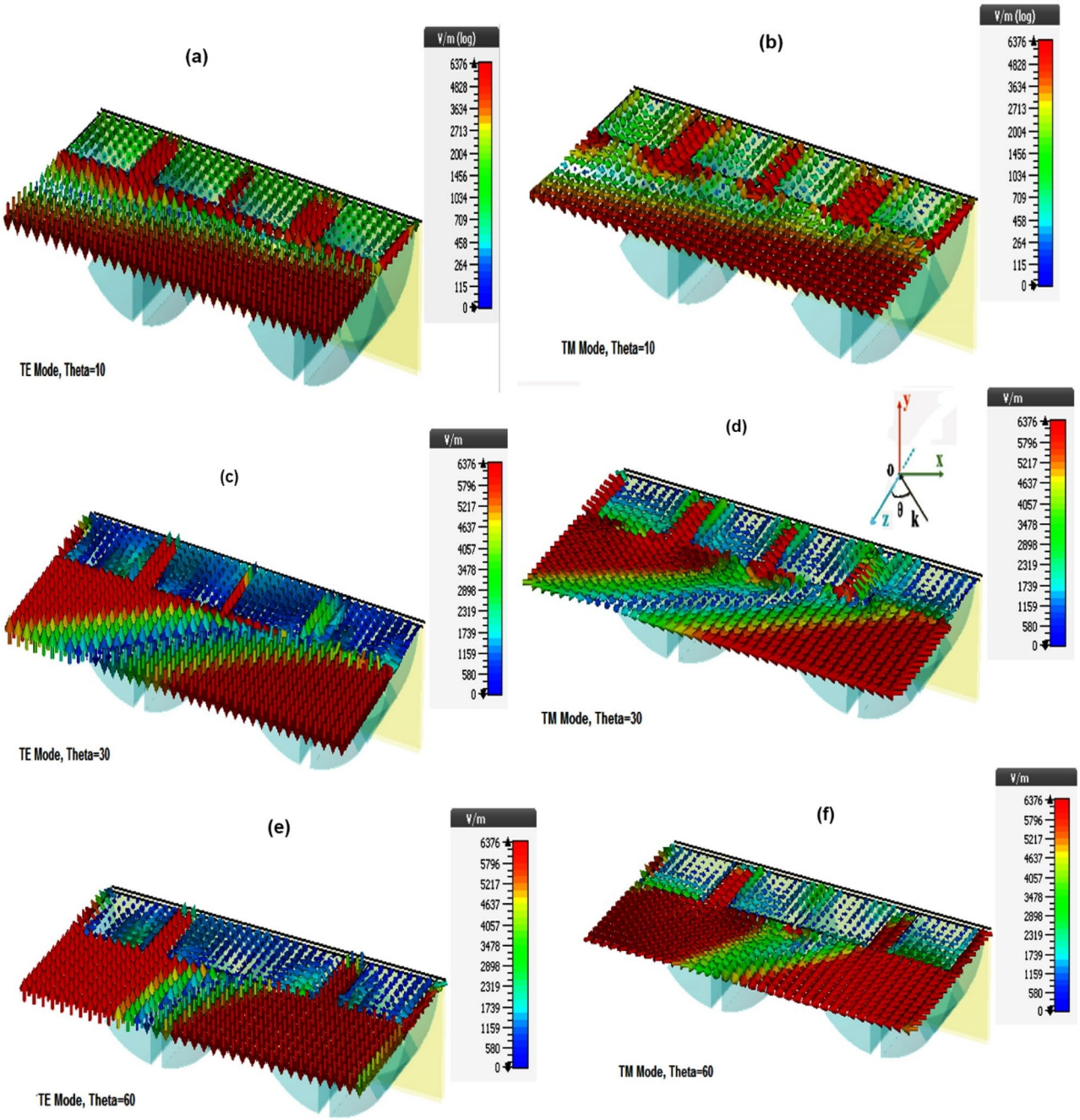

Figure 9. E-field distributions of different oblique incidence at the central frequency (220 GHz) for (**a**) Theta = 10, TE Mode (**b**) Theta = 10, TM Mode (**c**) Theta = 30, TE Mode (**d**) Theta = 30, TM Mode (**e**) Theta = 60, TE Mode (**f**) Theta = 60, TM Mode.

MOST WIEDZY Downloaded from mostwiedzy.pl

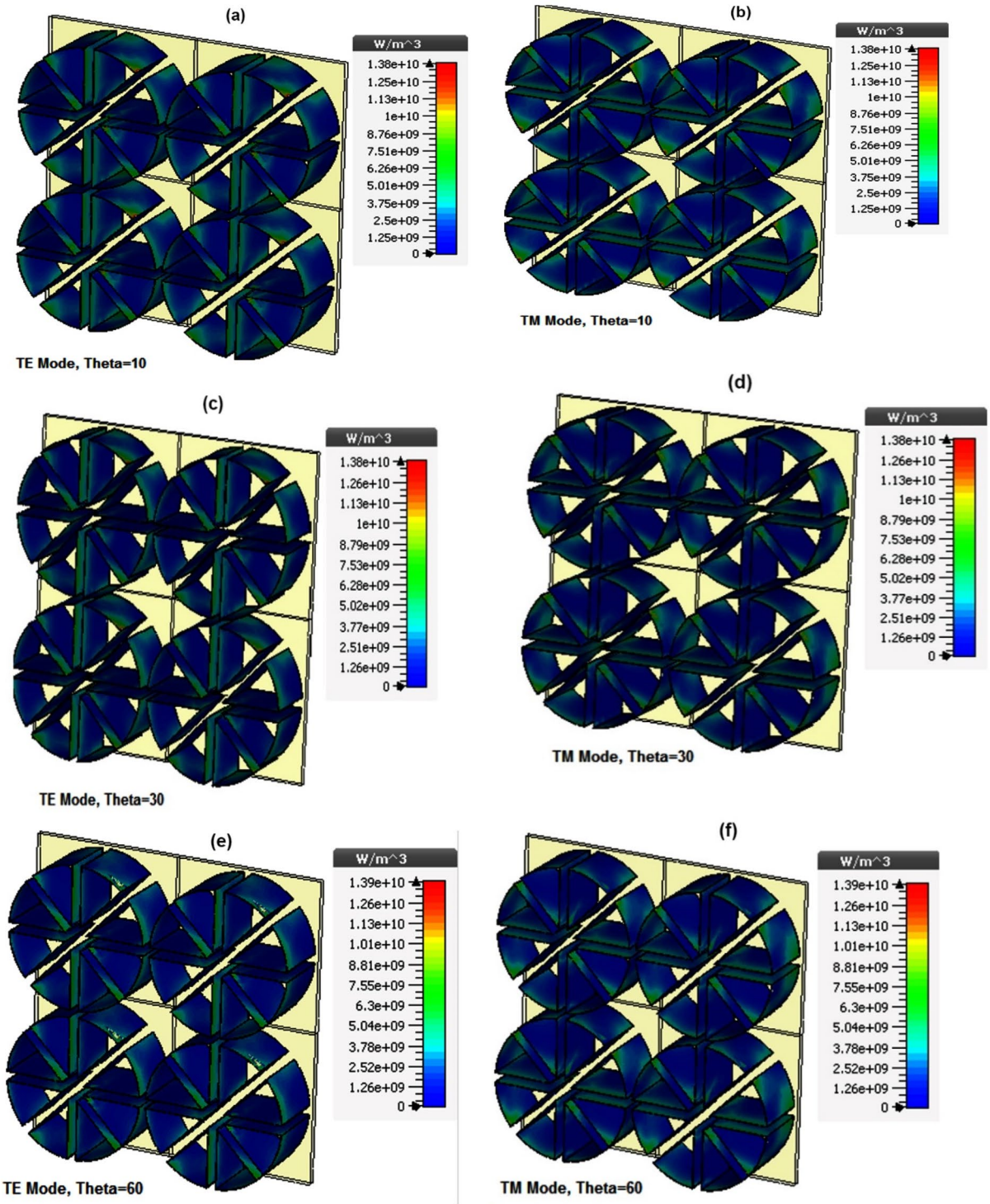

Figure 10. Power loss density based on oblique incidence at the central frequency (220 GHz) for (**a**) Theta = 10, TE Mode (**b**) Theta = 10, TM Mode (**c**) Theta = 30, TE Mode (**d**) Theta = 30, TM Mode (**e**) Theta = 60, TE Mode (**f**) Theta = 60, TM Mode.

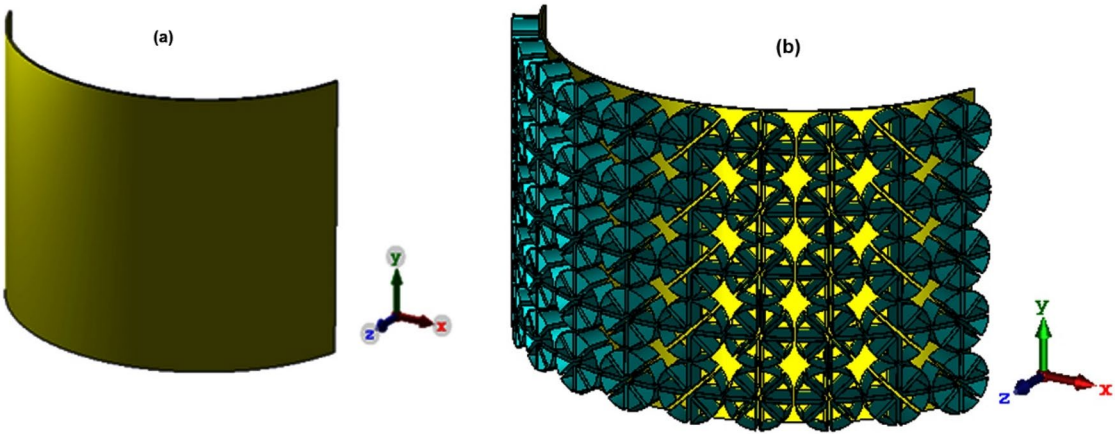

Figure 11. Curved structure (**a**) without and (**b**) with the proposed absorber.

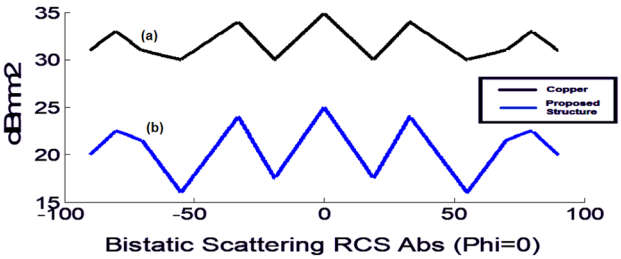

Figure 12. Curved structure (**a**) without and (**b**) with the proposed absorber.

References	BW (%)	Frequency band (GHz)	Unit cell volume (λ × λ × λ)	Maximum incident angle with greater 85% absorption		Polarization sensitivity (yes/no)	Configuration
				TE mode	TM mode		
[81]	44	58.6–91.4	0.64 × 0.64 × 0.64	30	90	No	U shaped resistive film
[82]	100	3.9–12	0.32 × 0.32 × 0.12	45	45	No	Carbon-loaded acrylonitrile butadiene styrene (ABS) polymer
[83]	150	5.1–40	0.5 × 0.5 × 0.17	55	70	No	Flaky carbonyl iron and polyther
Proposed structure	167	35–400	0.33 × 0.33 × 0.14	60	90	No	Graphite film

Table 1. Comparison of proposed absorber with previous works.

Data availability

The datasets used and/or analyzed during the current study are available from the corresponding author upon reasonable request.

Received: 20 June 2022; Accepted: 11 January 2023
Published online: 19 January 2023

References

1. Pendry, J. B. *et al.* Magnetism from conductors and enhanced nonlinear phenomena. *IEEE Trans. Microw. Theory Tech.* **47**(11), 2075–2084 (1999).
2. Liu, X. *et al.* Taming the blackbody with infrared metamaterials as selective thermal emitters. *Phys. Rev. Lett.* **107**, 45901 (2011).
3. Reinhard, B. *et al.* Metamaterial near-field sensor for deep-subwavelength thickness measurements and sensitive refractometry in the terahertz frequency range. *Appl. Phys. Lett.* **100**(22), 221101 (2012).
4. Watts, C. M. *et al.* Terahertz compressive imaging with metamaterial spatial light modulators. *Nat. Photon.* **8**(8), 605 (2014).
5. Han, T. *et al.* Full control and manipulation of heat signatures: Cloaking, camouflage and thermal metamaterials. *Adv. Mater.* **26**(11), 1731–1734 (2014).
6. Wu, C. *et al.* Metamaterial-based integrated plasmonic absorber/emitter for solar thermo-photovoltaic systems. *J. Opt.* **14**(2), 024005 (2012).

MOST WIEDZY Downloaded from mostwiedzy.pl

7. Wang, Y. *et al.* Perfect control of diffraction patterns with phase-gradient metasurfaces. *ACS Appl. Mater. Interfaces* **14**(14), 16856–16865 (2022).
8. Yuan, Y. *et al.* A fully phase-modulated metasurface as an energy-controllable circular polarization router. *Adv. Sci.* **7**(18), 2001437 (2020).
9. Jiang, D. *et al.* The development of a wideband and angle-insensitive metamaterial filter with extraordinary infrared transmission for micro-thermophotovoltaics. *J. Mater. Chem. C* **3**(15), 3552–3558 (2015).
10. Si, L.-M. & Lv, X. CPW-FED multi-band omni-directional planar microstrip antenna using composite metamaterial resonators for wireless communications. *Prog. Electromagn. Res.* **83**, 133–146 (2008).
11. Xu, H.-X. *et al.* A metamaterial antenna with frequency-scanning omnidirectional radiation patterns. *Appl. Phys. Lett.* **101**(17), 173501 (2012).
12. Planck, M. Ueber das gesetz der energieverteilung im normalspectrum. *Ann. Phys.* **309**(3), 553–563 (1901).
13. Wang, B.-X. *et al.* Broadband, polarization-insensitive and wide-angle terahertz metamaterial absorber. *Phys. Scr.* **89**(11), 115501 (2014).
14. Lee, Y. P. *et al. Metamaterials for Perfect Absorption*, vol. 236. (Springer, 2016).
15. Khuyen, B. X. *et al.* Size-efficient metamaterial absorber at low frequencies: Design, fabrication, and characterization. *J. Appl. Phys.* **117**(24), 243105 (2015).
16. Dung, N. *et al.* Perfect and broad absorption by the active control of electric resonance in metamaterial. *J. Opt.* **17**(4), 045105 (2015).
17. Chaurasiya, D. *et al.* An ultrathin quad-band polarization-insensitive wide-angle metamaterial absorber. *Microw. Opt. Technol. Lett.* **57**(3), 697–702 (2015).
18. Lee, D. *et al.* Incident angle-and polarization-insensitive metamaterial absorber using circular sectors. *Sci. Rep.* **6**, 27155 (2016).
19. Torabi, E. S., Fallahi, A. & Yahaghi, A. Evolutionary optimization of graphene-metal metasurfaces for tunable broadband terahertz absorption. *IEEE Trans. Antennas Propag.* **65**(3), 1464–1467 (2017).
20. Lalbakhsh, A., Afzal, M. U. & Esselle, K. P. Multi-objective particle swarm optimization to design a time delay equalizer metasurface for an electromagnetic band gap resonator antenna. *IEEE Antennas Wirel. Propag. Lett.* **16**, 912–915 (2017).
21. Lalbakhsh, A. *et al. Design of an Artificial Magnetic Conductor Surface Using an Evolutionary Algorithm*. In *Proc. Int. Conf. Electromagnetics in Advanced Applications (ICEAA)*.
22. Sattari, M. A., Hanus, R. & Nazemi, E. Applicability of time-domain feature extraction methods and artificial intelligence in two-phase flow meters based on gamma-ray absorption technique. *Measurement* **168**, 108474 (2021).
23. Phan, G. *et al.* Combination of X-ray tube and GMDH neural network as a nondestructive and potential technique for measuring characteristics of gas–oil–water three phase flows. *Measurement* **168**, 108427 (2021).
24. Faraj, R. H. *et al.* Proposing a gamma radiation based intelligent system for simultaneous analyzing and detecting type and amount of petroleum by-products. *Nucl. Eng. Technol.* **53**(4), 1277–1283 (2021).
25. Ali, P. J. M. *et al.* Application of GMDH neural network technique to improve measuring precision of a simplified photon attenuation based two-phase flowmeter. *Flow Meas. Instrum.* **75**, 101804 (2020).
26. Nazemi, E. *et al.* Online measuring density of oil products in annular regime of gas-liquid two phase flows. *Measurement* **129**, 296–301 (2018).
27. Hanus, R. *et al.* Density and velocity determination for single-phase flow based on radiotracer technique and neural networks. *Flow Meas. Instrum.* **61**, 9–14 (2018).
28. Roshani, G., Nazemi, E. & Roshani, M. Flow regime independent volume fraction estimation in three-phase flows using dual-energy broad beam technique and artificial neural network. *Neural Comput. Appl.* **28**(1), 1265–1274 (2017).
29. Nazemi, E. *et al.* Intelligent recognition of gas–oil–water three-phase flow regime and determination of volume fraction using radial basis function. *Flow Meas. Instrum.* **54**, 39–45 (2017).
30. Feghhi, S. *et al.* Investigation of using 60Co source and one detector for determining the flow regime and void fraction in gas–liquid two-phase flows. *Flow Meas. Instrum.* **50**, 73–79 (2016).
31. Setayeshi, S. *et al.* Flow regime identification and void fraction prediction in two-phase flows based on gamma ray attenuation. *Measurement* **62**, 25–32 (2015).
32. Lalbakhsh, P., Zaeri, B. & Lalbakhsh, A. An improved model of ant colony optimization using a novel pheromone update strategy. *IEICE Trans. Inf. Syst.* **E96-D**(11), 2309–2318 (2013).
33. Lalbakhsh, P. *et al*. Antnet with reward-penalty reinforcement learning. In *2010 2nd International Conference on Computational Intelligence, Communication Systems and Networks*.
34. Roshani, M. *et al.* Evaluation of flow pattern recognition and void fraction measurement in two phase flow independent of oil pipeline's scale layer thickness. *Alex. Eng. J.* **60**(1), 1955–1966 (2021).
35. Karami, A. *et al.* Enhancing the performance of a dual-energy gamma ray based three-phase flow meter with the help of grey wolf optimization algorithm. *Flow Meas. Instrum.* **64**, 164–172 (2018).
36. Karambasti, B. M. *et al.* Design methodology and multi-objective optimization of small-scale power-water production based on integration of Stirling engine and multi-effect evaporation desalination system. *Desalination* **526**, 115542 (2022).
37. Johanesson, D. O., Koziel, S. & Bekasiewicz, A. EM-driven constrained miniaturization of antennas using adaptive in-band reflection acceptance threshold. *Int. J. Numer. Model. Electron. Netw. Devices Fields* **32**(2), e2513 (2019).
38. Bekasiewicz, A. & Koziel, S. Reliable multistage optimization of antennas for multiple performance figures in highly dimensional parameter spaces. *IEEE Antennas Wirel. Propag. Lett.* **18**(7), 1522–1526 (2019).
39. Koziel, S., Pietrenko-Dabrowska, A. & Plotka, P. Design specification management with automated decision-making for reliable optimization of miniaturized microwave components. *Sci. Rep.* **12**(1), 1–14 (2022).
40. Koziel, S. & Pietrenko-Dabrowska, A. Constrained multi-objective optimization of compact microwave circuits by design triangulation and pareto front interpolation. *Eur. J. Oper. Res.* **299**(1), 302–312 (2022).
41. Abdollahi, M. & Parandin, F. A novel structure for realization of an all-optical, one-bit half-adder based on 2D photonic crystals. *J. Comput. Electron.* **18**(4), 1416–1422 (2019).
42. Parandin, F. *et al.* Design of a high bitrate optical decoder based on photonic crystals. *J. Comput. Electron.* **17**(2), 830–836 (2018).
43. Saghaei, H. *et al.* Line defects on As2Se3-Chalcogenide photonic crystals for the design of all-optical power splitters and digital logic gates. *Superlattices Microstruct.* **110**, 133–138 (2017).
44. Parandin, F. & Karkhanehchi, M. M. Terahertz all-optical NOR and AND logic gates based on 2D photonic crystals. *Superlattices Microstruct.* **101**, 253–260 (2017).
45. Karkhanehchi, M. M., Parandin, F. & Zahedi, A. Design of an all optical half-adder based on 2D photonic crystals. *Photon Netw. Commun.* **33**(2), 159–165 (2017).
46. Roshani, S. & Roshani, S. A compact coupler design using meandered line compact microstrip resonant cell (MLCMRC) and bended lines. *Wirel. Netw.* **27**(1), 677–684 (2021).
47. Bavandpour, S. K. *et al.* A compact lowpass-dual bandpass diplexer with high output ports isolation. *AEU Int. J. Electron. Commun.* **135**, 153748 (2021).
48. Roshani, S. & Roshani, S. Design of a compact LPF and a miniaturized Wilkinson power divider using aperiodic stubs with harmonic suppression for wireless applications. *Wirel. Netw.* **26**(2), 1493–1501 (2020).
49. Ahmadi, A. *et al.* A novel dual-mode wideband band pass filter. *Appl. Comput. Electromagn. Soc. J. (ACES J.)* **29**(9), 735–742 (2014).

50. Lalbakhsh, A. *et al.* A compact C-band bandpass filter with an adjustable dual-band suitable for satellite communication systems. *Electronics* **9**(7), 1088–1088 (2020).
51. Lalbakhsh, A. *et al.* A design of a dual-band bandpass filter based on modal analysis for modern communication systems. *Electronics* **9**(11), 1770–1770 (2020).
52. Parandin, F., Kamarian, R. & Jomour, M. Optical 1-bit comparator based on two-dimensional photonic crystals. *Appl. Opt.* **60**(8), 2275–2280 (2021).
53. Parandin, F., Kamarian, R. & Jomour, M. A novel design of all optical half-subtractor using a square lattice photonic crystals. *Opt. Quant. Electron.* **53**(2), 1–10 (2021).
54. Parandin, F. & Malmir, M. Low delay time all optical NAND, XNOR and OR Logic gates based on 2D photonic crystal structure. *J. Electr. Comput. Eng. Innov. JECEI* **8**(1), 1–8 (2020).
55. Vahdati, A. & Parandin, F. Antenna patch design using a photonic crystal substrate at a frequency of 1.6 THz. *Wirel. Pers. Commun.* **109**(4), 2213–2219 (2019).
56. Parandin, F. High contrast ratio all-optical 4× 2 encoder based on two-dimensional photonic crystals. *Opt. Laser Technol.* **113**, 447–452 (2019).
57. Pirasteh, A., Roshani, S. & Roshani, S. Design of a miniaturized class F power amplifier using capacitor loaded transmission lines. *Frequenz* **74**(3–4), 145–152 (2020).
58. Lotfi, S., Roshani, S. & Roshani, S. Design of a miniaturized planar microstrip Wilkinson power divider with harmonic cancellation. *Turk. J. Electr. Eng. Comput. Sci.* **28**(6), 3126–3136 (2020).
59. Hookari, M., Roshani, S. & Roshani, S. Design of a low pass filter using rhombus-shaped resonators with an analytical LC equivalent circuit. *Turk. J. Electr. Eng. Comput. Sci.* **28**(2), 865–874 (2020).
60. Hookari, M., Roshani, S. & Roshani, S. High-efficiency balanced power amplifier using miniaturized harmonics suppressed coupler. *Int. J. RF Microw. Comput. Aided Eng.* **30**(8), e22252 (2020).
61. Roshani, S., Roshani, S. & Zarinitabar, A. A modified Wilkinson power divider with ultra harmonic suppression using open stubs and lowpass filters. *Analog Integr. Circ. Sig. Process* **98**(2), 395–399 (2019).
62. Roshani, S. & Roshani, S. Design of a very compact and sharp bandpass diplexer with bended lines for GSM and LTE applications. *AEU Int. J. Electron. Commun.* **99**, 354–360 (2019).
63. Goudarzi, A., Honari, M. M. & Mirzavand, R. A high-gain leaky-wave antenna using resonant cavity structure with unidirectional frequency scanning capability for 5G applications. *IEEE Access* **9**, 138858–138865 (2021).
64. Goudarzi, A., Honari, M. & Mirzavand, R. A millimeter-wave Fabry–Perot cavity antenna with unidirectional beam scanning capability for 5G applications. *IEEE Trans. Antennas Propag.* **70**, 1787–1796 (2021).
65. Karimi, G. *et al.* Design of modified Z-shaped and T-shaped microstrip filter based on transfer function analysis. *Wirel. Pers. Commun.* **82**(4), 2005–2016 (2015).
66. Lalbakhsh, A. *et al.* Advancements and artificial intelligence approaches in antennas for environmental sensing. In *Artificial Intelligence and Data Science in Environmental Sensing* 19–38 (2022).
67. Torabi, Y. *et al.* A wide-angle scanning sub-Terahertz Leaky-wave antenna based on a multilayer dielectric image waveguide. *Electronics* **10**(17), 2172 (2021).
68. Paul, G. S., Mandal, K. & Lalbakhsh, A. Single-layer ultra-wide stop-band frequency selective surface using interconnected square rings. *AEU Int. J. Electron. Commun.* **132**, 153630–153630 (2021).
69. Adibi, S., Honarvar, M. A. & Lalbakhsh, A. Gain enhancement of wideband circularly polarized UWB antenna using FSS. *Radio Sci.* **56**(1), e2020RS007098 (2021).
70. Lalbakhsh, A. *et al.* All-metal wideband frequency-selective surface bandpass filter for TE and TM polarizations. *IEEE Trans. Antennas Propag.* **70**, 2790–2800 (2022).
71. Lalbakhsh, A. *et al.* Design of a compact planar transmission line for miniaturized rat-race coupler with harmonics suppression. *IEEE Access* **9**, 129207–129217 (2021).
72. Lalbakhsh, A. *et al. A High-Gain Wideband EBG Resonator Antenna for 60 GHz Unlicenced Frequency Band*.
73. Lalbakhsh, A. *et al.* Low-cost non-uniform metallic lattice for rectifying aperture near-field of electromagnetic bandgap resonator antennas. *IEEE Trans. Antennas Propag.* **68**(5), 3328–3335 (2020).
74. Liu, Y. *et al.* Independently tunable multi-band and ultra-wide-band absorbers based on multilayer metal-graphene metamaterials. *Opt. Express* **27**(5), 7393–7404 (2019).
75. Nguyen, T. T. & Lim, S. Wide incidence angle-insensitive metamaterial absorber for both TE and TM polarization using eight-circular-sector. *Sci. Rep.* **7**(1), 3204 (2017).
76. Shen, X. *et al.* Polarization-independent wide-angle triple-band metamaterial absorber. *Opt. Express* **19**(10), 9401–9407 (2011).
77. Chen, S. *et al.* Polarization insensitive and omnidirectional broadband near perfect planar metamaterial absorber in the near infrared regime. *Appl. Phys. Lett.* **99**(25), 253104 (2011).
78. Koziel, S. & Pietrenko-Dabrowska, A. Rapid multi-criterial antenna optimization by means of pareto front triangulation and interpolative design predictors. *IEEE Access* **9**, 35670–35680 (2021).
79. Pietrenko-Dabrowska, A., Koziel, S. & Al-Hasan, M. Expedited yield optimization of narrow-and multi-band antennas using performance-driven surrogates. *IEEE Access* **8**, 143104–143113 (2020).
80. Liu, Y., Cheng, Q. S. & Koziel, S. A generalized SDP multi-objective optimization method for EM-based microwave device design. *Sensors* **19**(14), 3065 (2019).
81. Tang, J. *et al.* A polarization insensitive and broadband metamaterial absorber based on three-dimensional structure. *Opt. Commun.* **372**, 64–70 (2016).
82. Shen, Y. *et al.* An extremely wideband and lightweight metamaterial absorber. *J. Appl. Phys.* **117**(22), 224503 (2015).
83. Ye, D. *et al.* Ultrawideband dispersion control of a metamaterial surface for perfectly-matched-layer-like absorption. *Phys. Rev. Lett.* **111**(18), 187402 (2013).

Acknowledgements
This work is partially supported by the Icelandic Centre for Research (RANNIS) Grant 206606 and by National Science Centre of Poland Grant 2020/37/B/ST7/01448.

Author contributions
All authors contribute equally.

Competing interests
The authors declare no competing interests.

Additional information
Correspondence and requests for materials should be addressed to A.L.

MOST WIEDZY Downloaded from mostwiedzy.pl

Reprints and permissions information is available at www.nature.com/reprints.

Publisher's note Springer Nature remains neutral with regard to jurisdictional claims in published maps and institutional affiliations.

Open Access This article is licensed under a Creative Commons Attribution 4.0 International License, which permits use, sharing, adaptation, distribution and reproduction in any medium or format, as long as you give appropriate credit to the original author(s) and the source, provide a link to the Creative Commons licence, and indicate if changes were made. The images or other third party material in this article are included in the article's Creative Commons licence, unless indicated otherwise in a credit line to the material. If material is not included in the article's Creative Commons licence and your intended use is not permitted by statutory regulation or exceeds the permitted use, you will need to obtain permission directly from the copyright holder. To view a copy of this licence, visit http://creativecommons.org/licenses/by/4.0/.

© The Author(s) 2023